Automated detection of microfossil fish teeth from slide images using combined deep learning models

Kazuhide Mimura[a,b], Shugo Minabe[c], Kentaro Nakamura[c,a*], Kazutaka Yasukawa[b,c], Junichiro Ohta[b,c,a], Yasuhiro Kato[b,c,a,d]

[a]Ocean Resources Research Center for Next Generation, Chiba Institute of Technology, 2-17-1 Tsudanuma, Narashino, Chiba 275-0016, Japan.

[b]Frontier Research Center for Energy and Resources, School of Engineering, University of Tokyo, 7-3-1 Hongo, Bunkyo-ku, Tokyo 113-8656, Japan.

[c]Department of Systems Innovation, School of Engineering, The University of Tokyo, 7-3-1 Hongo, Bunkyo-ku, Tokyo 113-8656, Japan.

[d]Submarine Resources Research Center, Research Institute for Marine Resources Utilization, Japan Agency for Marine-Earth Science and Technology (JAMSTEC), 2-15 Natsushima-cho, Yokosuka, Kanagawa 237-0061, Japan.

Corresponding author:

Kentaro Nakamura

Department of Systems Innovation, School of Engineering, University of Tokyo,

7-3-1 Hongo, Bunkyo-ku, Tokyo 113-8656, Japan

Telephone: +81-3-5841-7089

E-mail: kentaron@sys.t.u-tokyo.ac.jp

Note: This is a non-peer reviewed preprint submitted to EarthArXiv

Authorship contribution statement

Conceptualization, KM, SM, and KN; program coding, KM, SM; preparation of the dataset, KM and SM; investigation, KM and JO; writing—original draft preparation, KM KN and KY; writing—review and editing, all authors; supervision, KN, and YK; funding acquisition, KM, KN, KY, and YK. All the authors have read and agreed to the published version of the manuscript.

ABSTRACT

Microfossil fish teeth, known as ichthyoliths, provide a key constraint on the depositional age and environment of deep-sea sediments, especially pelagic clays where siliceous and calcareous microfossils are rarely observed. However, traditional methods for the observation of ichthyoliths require considerable time and manual labor, which can hinder their wider application. In this study, we constructed a system to automatically detect ichthyoliths in microscopic images by combining two open source deep learning models. First, the regions for ichthyoliths within the microscopic images are predicted by the instance segmentation model Mask R-CNN. All the detected regions are then re-classified using the image classification model EfficientNet-V2 to determine the classes more accurately. Compared with only using the Mask R-CNN model, the combined system offers significantly higher performance (89.0% precision, 78.6% recall, and an F1 score of 83.5%), demonstrating the utility of the system. Our system can also predict the lengths of the teeth that have been detected, with more than 90% of the predicted lengths being within ± 20% of measured length. This system provides a novel, automated, and reliable approach for the detection and length measurement of ichthyoliths from microscope images that can be applied in a range of paleoceanographic and paleoecological contexts.

Keywords:

Deep learning;

Object detection;

Image classification;

Microfossils;

Ichthyolith

1. Introduction

Pelagic clay is a type of deep-sea sediment that covers more than one-third of the global ocean floor (Dutkiewicz et al., 2015) and has long been regarded as an important medium for recording changes in atmospheric and oceanic circulation, surface ocean productivity, and the influx of extraterrestrial material in the pelagic realm (Kyte et al., 1993; Kyte, 1998; Kyte and Bostwick, 1995; Nozaki et al., 2019; Tanaka et al., 2022; Zhou and Kyte, 1992). The chemical composition of pelagic clay varies considerably despite its homogenous appearance, reflecting the fractions of its components, such as terrigenous dust, volcanic materials, hydrogenous and hydrothermal Fe-Mn oxides, and biogenic components (Dunlea et al., 2015a, 2015b; Leinen, 1987; Ren et al., 2021; Tanaka et al., 2022; Yasukawa et al., 2016, 2019; Ziegler et al., 2007).

Pelagic clay has recently received attention as a novel type of mineral resource for rare-earth elements and yttrium (REY), which are industrially critical metals, especially for technologies and products aiming toward carbon-neutrality. Pelagic clays enriched in REY, termed as “REY-rich mud” (Kato et al., 2011), were originally discovered in the deep-sea basin of the central North and eastern South Pacific Ocean. To date, they have been reported from the global ocean, including the western North Pacific (Bi et al., 2021; Fujinaga et al., 2016; Tanaka et al., 2020a, 2020b), central and South Pacific (Ohta et al., 2021; Sa et al., 2018; Zhou et al., 2020, 2021), Indian (Yasukawa et al., 2014, 2015; Yu et al., 2021; Zhang et al., 2017) and Atlantic Oceans (Menendez et al., 2017; Nakamura et al., 2015). Notably, the existence of "extremely REY-rich mud" in the western North Pacific Ocean (Iijima et al., 2016; Mimura et al., 2019; Takaya et al., 2018), together with the investigations of physical beneficiation techniques (Takaya et al., 2018) and by-product metal extraction (Yasukawa et al., 2018, 2020), further highlights the significance of pelagic clay as a promising mineral resource. Interestingly, the accumulation of REY in pelagic clay was caused by changes in bioproductivity and ocean circulation, which reflects changes in the Earth's climate system (Ohta et al., 2020). This indicates that examining environmental changes recorded in pelagic clay is essential for understanding the genesis and distribution of industrially critical metal resources, emphasizing the increasing importance of analyzing pelagic clay.

Depositional age is key information for understanding depositional environments of the seafloor sediment because the environment has been affected by a secular change in global climate (Westerhold et al., 2020; Zachos et al., 2008) and plate motion over geologic timescales (Müller et al., 2018). However, calcareous or siliceous microfossils, which have commonly been used for constraining depositional ages of the seafloor sediment, are not found in pelagic clay, owing to the dissolution of the fossils by undersaturation of carbonates and silica in the deep-sea environment. This has hampered examination of the depositional environment and exploration of the origin that controls distribution of deep-sea resources.

In contrast, fish teeth and denticles, known as ichthyoliths, are well preserved in almost all kinds of seafloor sediments because they are composed of calcium phosphate, which is not easily dissolved (Sibert et al., 2014). Therefore, ichthyoliths have been used as a key for constraining the depositional age of pelagic clay (Doyle et al., 1974; Doyle and Riedel, 1979, 1985; Ohta et al., 2020). In addition, ichthyoliths are regarded as indicators of depositional environments recently. The productivity of pelagic fish has been measured based on the accumulation rate of ichthyoliths (Sibert et al., 2014, 2016, 2020; Sibert and Rubin, 2021), the evolution of pelagic ecosystems has been explored based on variations in morphotypes (Sibert et al., 2018; Sibert and Rubin, 2021), and the distribution of pelagic fish has been studied based on variation in the length of fish teeth (Britten and Sibert, 2020). Hence, establishing an effective method for ichthyolith observation will enable understanding of the records on the evolution of pelagic realms which has long been a black box in Earth science.

Traditionally, ichthyolith analysis first involves extracting coarse-grained particles from the target sediment. By observing these grains under a stereomicroscope, ichthyoliths are manually picked up and moved on to a slide using a fine-pointed brush. This process, called 'handpicking', remains a common technique for both stratigraphic and environmental research (Ohta et al., 2020; Sibert et al., 2017) and is one of the most time-consuming processes in ichthyolith analysis. Slides with the ichthyoliths are then observed under a microscope for detailed description and identification. Observers describe a range of features including their outer shape, inner structures, and size (Britten and Sibert, 2020; Doyle and Riedel, 1979; Sibert et al., 2018), which also requires considerable time and effort by experienced experts.

In comparison to these manual techniques, recent developments in computer vision have achieved promising results in various fields including medicine, neuroscience, and robotics (Jo et al., 2017; Kim et al., 2018; Sakai et al., 2018; Shoji et al., 2018; Suleymanova et al., 2018). Techniques in computer vision have also been applied in the field of microfossil research for the tasks of classification and detection. The classification of microfossils was first attempted by obtaining key morphological parameters from microfossil images (Marmo et al., 2006; Yu et al., 1996), with support vector machines (SVMs) contributing to their classification according to the acquired values (Apostol et al., 2016; Bi et al., 2015; Hu and Davis, 2005; Solano et al., 2018; Xu et al., 2020). Owing to the development of convolutional neural networks (CNNs), deep learning based classification models have successfully been used to determine the taxa of various microfossils including foraminifera and radiolarians (Carvalho et al., 2020; Hsiang et al., 2019; Itaki et al., 2020; Keçeli et al., 2017; Marchant et al., 2020; Mitra et al., 2019; Pires de Lima et al., 2020; Xu et al., 2020). Although some of these classification models achieve an accuracy of > 85% (Hsiang et al., 2019; Itaki et al., 2020; Marchant et al., 2020), large training datasets are often required, which creates the challenge of generating a large number of images for each microfossil species. To address this problem, previous studies (Hsiang et al., 2018; Itaki et al., 2020; Tetard et al., 2020) have proposed a method that captures the entire area of a slide. In these studies, individual particles were extracted from the image based on thresholding, which may reduce the efficiency of ichthyoliths observations for the following two reasons. First, particles have to be positioned on the imaged slides without overlap, which can be practically difficult when using glass slides. Second, ichthyoliths are translucent when observed under a polarized light microscope, which makes determining an appropriate threshold challenging.

Here, as a first step toward using deep learning for ichthyolith observation, we describe a deep learning based system that can detect microfossil fish teeth from glass slide images and predict their lengths. The system is composed of open-source libraries, so that it can be readily applied to a range of detection problems within the geosciences.

2. Materials and Methods

2.1. System overview

Our system is divided into two parts: (1) the detection of fossil fish teeth from slide images and (2) the precise classification of the detected particles (Fig. 1), each described in the following sections.

2.1.1 Detection using Mask R-CNN

The slide images are processed using the object detection model “Mask R-CNN.” Mask R-CNN is an open-source model that is capable of semantic segmentation and has a deep-learning-based algorithm that predicts the label in every pixel of an image (He et al., 2017). The input image size was set to 640 × 640 pixels.

2.1.2 Re-classification using EfficientNet-V2

Although the fully trained Mask R-CNN model can predict the classes of the objects detected, we found that the model was unable to learn the features of fish teeth with our dataset. Therefore, we combined it with another open source deep learning model, ‘EfficientNet-V2’ (Tan and Le, 2021), which discriminates the classes of the particles detected by the Mask R-CNN model. Images of particles detected by Mask R-CNN were resized to 224 × 224 pixels without changing the aspect. These images are then classified into ‘tooth’ or ‘noise’ classes by the trained EfficientNet-V2 model. The class determined by the image-classification model was taken as the final class predicted by the system. In other words, even if a particle was predicted as a “tooth” by the Mask R-CNN model, it was considered “noise” if it was classified as such by the EfficientNet-V2 model.

2.2 Experiments

2.2.1 Preparation of slide images

Glass slides were prepared from the pelagic clay samples collected at Ocean Drilling Program (ODP) Site 1179 and piston core site MR15-E01 PC11 in the western North Pacific Ocean, and Integrated Ocean Drilling Program (IODP) Sites U1366 and U1370 in the South Pacific Ocean. The locations and water depths of these sites are summarized in Table S1. The method for preparing the slides followed previous studies on the determination of depositional ages (Doyle and Riedel, 1985; Ohta et al., 2020) with some modifications as described by Sibert et al. (2017). Approximately 5 g of the wet sediment sample was first well mixed with deionized water in a plastic bottle, and then sieved through a 62 μm mesh to collect the larger particles. Heavy liquid separation was then used to concentrate biogenic calcium phosphate grains. The particles were well mixed with a solution of sodium polytungstate (SPT; specific gravity = 2.80−2.85 g/cm^3) and centrifuged at 1000−1500 rpm. The collected particles were washed with deionized water, placed on glass slides using a pipette, dried at 40 °C, and then sealed with a cover glass using a light-curing adhesive. Microscopic images of the entire area of the prepared slides were automatically captured using an RX-100 digital microscope (Hirox Co., Ltd.). This microscope has a motorized stage that moves gradually to divide the observation area into small squares, which can be continuously imaged. The magnification of the microscope was 200× (each pixel = 0.96 × 0.96 μm), and approximately 1000 images of 1200 × 1200 pixels were generated from a single slide.

2.2.2. Training of the object detection model

A total of 958 slide images with at least one ichthyolith were prepared to train the Mask R-CNN model. For these images, ichthyolith contour and class information was annotated using the VGG Image Annotator (Dutta and Zisserman, 2019). The dataset was randomly split into a training dataset, which was composed of 958 images with annotation data for 1625 teeth, and a validation dataset composed of 92 images and annotation data for 165 teeth.

The mask R-CNN model training was conducted using the online cloud service Paperspace (https://www.paperspace.com/). To augment the dataset, the images were randomly flipped upside down and/or left-to-right during the training. The initial learning rate was set at 0.001, and the model was trained for 80 epochs. The progress of learning was monitored by calculating the losses implemented in the Mask R-CNN library for both the training and validation datasets.

2.2.3. Training the image classification model

Particles within the slide images were trimmed from the classification model dataset. These particles were manually labeled into the ‘tooth’ and ‘noise’ classes. Examples of ‘noisy’ particles are fish bones, opaque grains that are possibly micro ferromanganese (Fe-Mn) oxides (Yasukawa et al., 2020), and the edges of light-curing adhesives (see Fig. 1b). The EfficientNet-V2 model was trained using the Google Colaboratory Cloud service (Carneiro et al., 2018). During the training, the images were randomly flipped upside down and/or left-to-right to prevent overfitting. The learning rate was set at 0.005, and the model was trained for 20 epochs. The progress of the learning was monitored by calculating the losses and accuracies for both the training and validation datasets.

2.2.4. Tests for the practical use of the system

In addition to the validation of each model, we conducted a practical test to verify the performance of the entire system. A total of 5177 slide images from six glass slides were generated from a single sample (ODP Site 1179, section 24, Core 5, 75−77 cm interval). This sample was not used for any of the training or validation datasets. Annotation data for the locations of the 431 teeth within the images were prepared. The images were first subjected to detection using the trained Mask R-CNN model. By comparing the annotated data and the model predictions, the number of true positives (TPs), false positives (FPs), and false negatives (FNs) were determined.

TPs represent the numbers of teeth that were correctly predicted as teeth by the model. FPs represent the numbers of non-teeth particles that were incorrectly predicted as teeth. FNs represent the numbers of teeth that were not detected by the model. Using these values, several evaluation parameters were calculated as follows:

$$\text{Precision} = \frac{TP}{TP + FP} \ldots (1)$$

$$\text{Recall} = \frac{TP}{TP + FN} \ldots (2)$$

$$\text{F1 score} = \frac{2(Precision \times Recall)}{Precision + Recall} \ldots (3)$$

Precision represents the extent to which the model misclassified particles as teeth. Recall represents the extent to which the model failed to detect teeth. The F1 score is the harmonic mean of precision and recall, indicating the overall balance of the model. After evaluation of the Mask R-CNN model detection results, all of the detected particles were re-classified using the EfficientNet-V2 model, and the precision, recall, and F1 scores were recalculated.

2.3 Measurement of ichthyolith length

The dimensions of ichthyoliths are key for their accurate classification. Here, we defined the length of a tooth as the perpendicular length from the apex of the outline to the lowest level (Fig. S1a) based on the traditional ichthyolith description system (Doyle and Riedel, 1979). Given that variation in tooth length can be used as an indicator of variation in the body sizes of pelagic fish (Britten and Sibert, 2020), we attempted to predict the lengths of teeth automatically, by approximating the detected contours of each tooth within a rectangle and measuring the length of the longest side (Fig. S1b). This approach was based on the assumption that most teeth have an elongated shape (Britten and Sibert, 2020). To evaluate the accuracy of the acquired lengths, tooth lengths were manually measured in the same images following the traditional methods for ichthyolith biostratigraphy.

3. Results and Discussion

3.1 Detection of fish teeth

3.1.1 Mask R-CNN

Figure 2 shows the trend of the loss function for each training epoch. Although the loss values for the training dataset gradually decreased, the loss for the validation dataset oscillated within the range of 0.5−1.2 and did not show any significant decrease. This indicates that the model could not sufficiently learn the general features of the teeth. A practical test was performed using the trained model up to epoch 80. Although the model showed 99.3% recall, the precision was 5.5%. Thus, while almost all of the ichthyoliths were correctly detected, many non-tooth particles were incorrectly classified as teeth by the trained Mask R-CNN model (see Fig. 1b). Therefore, detection by the Mask R-CNN model alone does not represent a time-saving approach because manual intervention is still needed to correctly identify ichthyoliths from a large number of detected particles.

3.1.2 EfficientNet-V2

The trends in the loss functions and accuracies for the training and validation datasets during each epoch of the EfficientNet-V2 model training are shown in Fig. 3. For the training data, there was a decrease in loss and an increase in accuracy up to epoch 20. The validation data also showed a decrease in loss and an increase in accuracy up to epoch 10, and maintained low losses and high accuracy without oscillation during epochs 10–20. This suggests that the model successfully learned the general features of the teeth without overfitting the training dataset. The model trained up to epoch 19 was selected as the best model, when the lowest validation loss was recorded, and was subjected to the practical test.

By combining the Mask R-CNN model trained up to epoch 80 and the EfficientNet-V2 model trained until epoch 19, the practical test was performed as described in Section 2.2.4. By testing several thresholding confidence scores, we found that the highest F1 value was achieved when the particles predicted by the EfficientNet-V2 model to be teeth, with a confidence of more than 0.45, were treated as teeth (Table S2). Compared to the Mask

R-CNN model alone, the combined system showed significantly higher precision and slightly lower recall (89.0% and 78.6%, respectively, Fig. 4). This indicates that the EfficientNet-V2 model is effective at identifying fish teeth from the large numbers of particles detected by the Mask R-CNN model. The F1 score was 83.5%, which is eight times higher than that of the Mask R-CNN model when used alone.

For application of this system in stratigraphic research, it is important to detect clear and distinct ichthyoliths with a small number of false positives, even if small and obscure ichthyoliths are not detected. In this case, a threshold score of 0.45 should be used to obtain the highest F1 score. In environmental research, the total number of ichthyoliths within a sample is an important proxy. A threshold score of 0.1 and manually checking the detection results can minimize the occurrence of false negatives. Although this approach requires some manual labor, it is much more time-efficient than the previous handpicking process.

3.2 Measurement of ichthyolith length

The scatter diagram for the lengths of the teeth predicted by the contours of the detection results and manually measured lengths is shown in Fig. 5. In three cases (out of 341), the predicted lengths were significantly shorter than the measured length, which occurred when the Mask R-CNN model was unable to determine the contours of the model. However, overall, the predicted lengths of 90.6% of the detected teeth were within ± 20% of their measured lengths. This indicates that as well as their detection and classification, our system provides an efficient means of determining the length distribution of fossil fish teeth.

3.3 Implications for the wider application of object detection in the geosciences

There are many fields within the geosciences in which images are used to detect and/or count target objects (Ohta et al., 2016, 2020; Takahashi et al., 2009; Usui et al., 2017). Automation of these tasks using object detection techniques has the potential to acquire a greater number of results and enable more comprehensive investigation than has been previously possible. However, object detection has not yet been widely applied in the geosciences, with the exception of remote sensing (Zhang et al., 2020). This can be attributed to the difficulty in generating the large learning datasets required for precise detection. This is hindered by the requirement for special equipment, such as microscopes (polarizing microscopy, stereoscopic microscopy, and scanning electron microscopy) and computed tomography (CT) scanners. This has cost, time, and manual labor implications that can make the acquisition of a large number of images impractical. Second, the annotation process of object detection often requires skilled expertise, compared with more applied fields of research such as robotics, medicine, and materials science, and devoting sufficient resources (both budgetary and personnel) to the annotation process may be less prioritized in this field.

Our study shows that a relatively small dataset (< 1000 microscopic images containing approximately 1800 teeth) is sufficient to train the Mask R-CNN model to detect the contours of possible teeth, although when used alone, it was not sufficient to distinguish the teeth precisely. Therefore, the best overall performance was achieved by fully training a model focused on the classification of the predicted regions, which requires much less time and manual labor than preparing a large dataset for the Mask R-CNN model. This indicates that challenging object detection problems can be efficiently addressed by dividing the task into two subtasks i.e., extracting the contours of candidate objects and then precisely classifying the objects based on the extracted contours. This implies that object detection may be applied in various fields in the geosciences, especially where the acquisition of large training datasets for object detection has proven to be challenging.

4. Conclusions

We developed and tested a system to detect fossil fish teeth from slide images by combining two open source deep learning models—the object detection model ‘Mask R-CNN’ and the image classification model ‘EfficientNet-V2’. The system provided results with 89.0% precision, 78.6% recall, and an F1 score of 83.5% in a test that assumed realistic conditions, indicating its potential for practical application. In addition, the system successfully derived the lengths of 90% of the detected teeth with an accuracy of ± 20%. As such, the system has potential for constraining both the depositional ages and environments of deep-sea sediments and, more broadly, contributing to research on the evolution of the marine ecosystem. Additional work is now being undertaken to update the EfficientNet-V2 model so that ichthyoliths can be further classified into morphological taxa. This requires a larger dataset of ichthyolith images, which could be compiled with the support of the system constructed in this study.

Competing interests

The authors declare that they have no competing interests.

Funding

This research was funded by the Japan Society for the Promotion of Science (JSPS) KAKENHI grant numbers 20H05658 to YK, 17H01361 to KN, 19J14560 and 21K20354 to KM.

Acknowledgements

The authors thank T. Itaki at the National Institute of Advanced Industrial Science and Technology for a preliminary discussion on the separation of ichthyoliths and the use of deep learning for microfossil observations. We would also like to thank A. Takeuchi, M. Shimbo, Y. Yoshikawa, and Y. Shigeto at Chiba Institute of Technology for their advice on developing deep learning models.

Data Availability

Datasets related to this article can be found at http://dx.doi.org/10.17632/zdpz6m9gzf.1, an open-source online data repository hosted at Mendeley Data (Mimura, 2022).

Code Availability

The sample codes for application of Mask R-CNN and EfficientNet-V2 for microfossils detection proble ms are on GitHub (https://github.com/KazuhideMimura/ai_ichthyolith; https://github.com/KazuhideMimura/e

NetV2_for_ai_ichthyolith).

References

Apostol, L.A., Márquez, E., Gasmen, P., Solano, G., 2016. RadSS: A radiolarian classifier using support vector machines, in: 7th International Conference on Information, Intelligence, Systems & Applications (IISA) 2016. IEEE Publications, pp. 1–6.

Bi, D., Shi, X., Huang, M., Yu, M., Zhou, T., Zhang, Y., Zhu, A., Shi, M., Fang, X., 2021. Geochemical and mineralogical characteristics of deep-sea sediments from the western North Pacific Ocean: Constraints on the enrichment processes of rare earth elements. Ore Geol. Rev. 138. 104318.

Bi, H., Guo, Z., Benfield, M.C., Fan, C., Ford, M., Shahrestani, S., Sieracki, J.M., 2015. A semi-automated image analysis procedure for in situ plankton imaging systems. PLOS ONE. 10, e0127121.

Britten, G.L., Sibert, E.C., 2020. Enhanced fish production during a period of extreme global warmth. Nat. Commun. 11, 5636.

Carneiro, T., Medeiros Da Nobrega, R.V., Nepomuceno, T., Bian, G., De Albuquerque, V.H.C., Filho, P.P.R., 2018. Performance analysis of google colaboratory as a tool for accelerating deep learning applications. IEEE Access. 6, 61677–61685.

Carvalho, L.E., Fauth, G., Baecker Fauth, S.B., Krahl, G., Moreira, A.C., Fernandes, C.P., Von Wangenheim, A., 2020. Automated microfossil identification and segmentation using a deep learning approach. Mar. Micropaleontol. 158. 101890.

Doyle, P.S., Kennedy, G.G., Riedel, W.R., 1974. Stratigraphy, in: Davies, T.A., Luyendyk, B.P., et al. (Eds.), Initial Reports of the Deep Sea Drilling Project 26, Washington (U.S. Government Printing Office), pp. 825–905.

Doyle, P.S., Riedel, W.R., 1979. Ichthyoliths: Present status of taxonomy and stratigraphy of microscopic fish skeletal debris. Scripps Institution Of Oceanography Reference Series. 79–16. Publications. National Technical Information Service, Springfield, Virginia, 22161, 1–231.

Doyle, P.S., Riedel, W.R., 1985. Cenozoic and Late Cretaceous ichthyoliths, in: Bolli, H.M., Saunders, J.B., Perch-Nielsen, K. (Eds.), Plankton Stratigraphy. Cambridge University Press, pp. 965–995.

Dunlea, A.G., Murray, R.W., Sauvage, J., Pockalny, R.A., Spivack, A.J., Harris, R.N., D'Hondt, S., 2015b. Cobalt-based age models of pelagic clay in the South Pacific Gyre. Geochem. Geophys. Geosyst. 16, 2694–2710.

Dunlea, A.G., Murray, R.W., Sauvage, J., Spivack, A.J., Harris, R.N., D'Hondt, S., 2015a. Dust, volcanic ash, and the evolution of the South Pacific Gyre through the Cenozoic. Paleoceanography. 30, 1078–1099.

Dutkiewicz, A., Müller, R.D., O'Callaghan, S., Jónasson, H., 2015. Census of seafloor sediments in the world's ocean. Geology. 43, 795–798.

Dutta, A., Zisserman, A., 2019. The via annotation software for images, audio and video, in: Proceedings of the 27th ACM International Conference on Multimedia, pp. 2276–2279.

Fujinaga, K., Yasukawa, K., Nakamura, K., Machida, S., Takaya, Y., Ohta, J., Araki, S., Liu, H., Usami, R., Maki, R., Haraguchi, S., Nishio, Y., Usui, Y., Nozaki, T., Yamazaki, T., Ichiyama, Y., Ijiri, A., Inagaki, F., Machiyama, H., Iijima, K., Suzuki, K., Kato, Y., KR13-02, MR13-E02 Leg 2, KR14-02 Cruise members., 2016. Geochemistry of REY-rich mud in the Japanese Exclusive Economic Zone around Minamitorishima Island. Geochem. J. 50, 575–590 Leg. 2.

He, K., Gkioxari, G., Dollar, P., Girshick, R., 2017. Mask R-CNN. IEEE Trans. Pattern Anal. Mach. Intell. 42, 386–397.

Hsiang, A.Y., Brombacher, A., Rillo, M.C., Mleneck-Vautravers, M.J., Conn, S., Lordsmith, S., Jentzen, A., Henehan, M.J., Metcalfe, B., Fenton, I.S., Wade, B.S., Fox, L., Meilland, J., Davis, C.V., Baranowski, U., Groeneveld, J., Edgar, K.M., Movellan, A., Aze, T., Dowsett, H.J., Miller, C.G., Rios, N., Hull, P.M., 2019. Endless Forams: > 34,000 modern planktonic foraminiferal images for taxonomic training and automated species recognition using convolutional neural networks. Paleoceanogr. Paleoclimatol. 34, 1157–1177.

Hsiang, A.Y., Nelson, K., Elder, L.E., Sibert, E.C., Kahanamoku, S.S., Burke, J.E., Kelly, A., Liu, Y., Hull, P.M.,

2018. AutoMorph: Accelerating morphometrics with automated 2D and 3D image processing and shape extraction. Methods Ecol. Evol. 9, 605–612.

Hu, Q., Davis, C., 2005. Automatic plankton image recognition with co-occurrence matrices and support vector machine. Mar. Ecol. Prog. Ser. 295, 21–31.

Iijima, K., Yasukawa, K., Fujinaga, K., Nakamura, K., Machida, S., Takaya, Y., Ohta, J., Haraguchi, S., Nishio, Y., Usui, Y., Nozaki, T., Yamazaki, T., Ichiyama, Y., Ijiri, A., Inagaki, F., Machiyama, H., Suzuki, K., Kato, Y., KR13-02 Cruise members, 2016. Discovery of extremely REY-rich mud in the western North Pacific Ocean. Geochem. J. 50, 557–573.

Itaki, T., Taira, Y., Kuwamori, N., Maebayashi, T., Takeshima, S., Toya, K., 2020. Automated collection of single species of microfossils using a deep learning–micromanipulator system. Prog. Earth Planet. Sci. 7, 1–7.

Jo, Y., Park, S., Jung, J., Yoon, J., Joo, H., Kim, M.H., Kang, S.J., Choi, M.C., Lee, S.Y., Park, Y., 2017. Holographic deep learning for rapid optical screening of anthrax spores. Sci. Adv. 3, e1700606.

Kato, Y., Fujinaga, K., Nakamura, K., Takaya, Y., Kitamura, K., Ohta, J., Toda, R., Nakashima, T., Iwamori, H., 2011. Deep-sea mud in the Pacific Ocean as a potential resource for rare-earth elements. Nat. Geosci. 4, 535–539.

Keçeli, A.S., Kaya, A., Keçeli, S.U., 2017. Classification of radiolarian images with hand-crafted and deep features. Comput. Geosci. 109, 67–74.

Kim, J., Cho, H., Hwangbo, M., Choi, J., Canny, J., Kwon, Y.P., 2018. Deep traffic light detection for self-driving cars from a large-scale dataset, in: 21st International Conference on Intelligent Transportation Systems (ITSC) 2018. IEEE Publications, pp. 280–285.

Kyte, F.T., 1998. A meteorite from the Cretaceous/Tertiary boundary. Nature. 396, 237–239.

Kyte, F.T., Bostwick, J.A., 1995. Magnesioferrite spinel in Cretaceous/Tertiary boundary sediments of the Pacific basin: Remnants of hot, early ejecta from the Chicxulub impact? Earth Planet. Sci. Lett. 132, 113–127.

Kyte, F.T., Leinen, M., Ross Heath, G.R., Zhou, L., 1993. Cenozoic sedimentation history of the central North Pacific: Inferences from the elemental geochemistry of core LL44-GPC3. Geochim. Cosmochim. Acta. 57, 1719–1740.

Leinen, M., 1987. The origin of paleochemical signatures in North Pacific pelagic clays: Partitioning experiments. Geochim. Cosmochim. Acta. 51, 305–319.

Marchant, R., Tetard, M., Pratiwi, A., Adebayo, M., de Garidel-Thoron, T., 2020. Automated analysis of foraminifera fossil records by image classification using a convolutional neural network. J. Micropalaeontol. 39, 183–202.

Marmo, R., Amodio, S., Cantoni, V., 2006. Microfossils shape classification using a set of width values, in: 18th International Conference on Pattern Recognition (ICPR'06) 1. IEEE Publications.

Menendez, A., James, R.H., Roberts, S., Peel, K., Connelly, D., 2017. Controls on the distribution of rare earth elements in deep-sea sediments in the North Atlantic Ocean. Ore Geol. Rev. 87, 100–113.

[dataset] Mimura, K., 2022. Datasets for ichthyolith detection, Mendeley Data, V1, doi: 10.17632/zdpz6m9gzf.1

Mimura, K., Nakamura, K., Yasukawa, K., Machida, S., Ohta, J., Fujinaga, K., Kato, Y., 2019. Significant impacts of pelagic clay on average chemical composition of subducting sediments: New insights from discovery of extremely rare-earth elements and yttrium-rich mud at Ocean Drilling Program Site 1149 in the western North Pacific Ocean. J. Asian Earth Sci. 186. 104059.

Mitra, R., Marchitto, T.M., Ge, Q., Zhong, B., Kanakiya, B., Cook, M.S., Fehrenbacher, J.S., Ortiz, J.D., Tripati, A., Lobaton, E., 2019. Automated species-level identification of planktic foraminifera using convolutional neural networks, with comparison to human performance. Mar. Micropaleontol. 147, 16–24.

Müller, R.D., Cannon, J., Qin, X., Watson, R.J., Gurnis, M., Williams, S., Pfaffelmoser, T., Seton, M., Russell, S.H.J., Zahirovic, S., 2018. GPlates: Building a virtual Earth through deep time. Geochem. Geophys. Geosyst. 19, 2243–2261.

Nakamura, K., Fujinaga, K., Yasukawa, K., Takaya, Y., Ohta, J., Machida, S., Haraguchi, S., Kato, Y., 2015. REY-rich mud: A deep-sea mineral resource for rare earths and yttrium, in: Handbook on the Physics and Chemistry of Rare Earths, Elsevier 46, pp. 79–127.

Nozaki, T., Ohta, J., Noguchi, T., Sato, H., Ishikawa, A., Takaya, Y., Kimura, J.I., Chang, Q., Shimada, K., Ishibashi, J.I., Yasukawa, K., Kimoto, K., Iijima, K., Kato, Y., 2019. A Miocene impact ejecta layer in the pelagic Pacific Ocean. Sci. Rep. 9, 16111.

Ohta, J., Yasukawa, K., Machida, S., Fujinaga, K., Nakamura, K., Takaya, Y., Iijima, K., Suzuki, K., Kato, Y., 2016. Geological factors responsible for REY-rich mud in the western North Pacific Ocean: Implications from mineralogy and grain size distributions. Geochem. J. 50, 591–603.

Ohta, J., Yasukawa, K., Nakamura, K., Fujinaga, K., Iijima, K., Kato, Y., 2021. Geological features and resource potential of deep-sea mud highly enriched in rare-earth elements in the Central Pacific Basin and the Penrhyn Basin. Ore Geol. Rev. 139. 104440.

Ohta, J., Yasukawa, K., Nozaki, T., Takaya, Y., Mimura, K., Fujinaga, K., Nakamura, K., Usui, Y., Kimura, J.I., Chang, Q., Kato, Y., 2020. Fish proliferation and rare-earth deposition by topographically induced upwelling at the Late Eocene cooling event. Sci. Rep. 10, 9896.

Pires de Lima, R., Welch, K.F., Barrick, J.E., Marfurt, K.J., Burkhalter, R., Cassel, M., Soreghan, G.S., 2020. Convolutional neural networks as an aid to biostratigraphy and micropaleontology: A test on Late Paleozoic microfossils. Palaios. 35, 391–402.

Ren, J., Liu, Y., Wang, F., He, G., Deng, X., Wei, Z., Yao, H., 2021. Mechanism and influencing factors of REY enrichment in deep-sea sediments. Minerals. 11, 196.

Sa, R., Sun, X., He, G., Xu, L., Pan, Q., Liao, J., Zhu, K.C., Deng, X., 2018. Enrichment of rare earth elements in siliceous sediments under slow deposition: A case study of the central North Pacific. Ore Geol. Rev. 94, 12–23.

Sakai, Y., Takemoto, S., Hori, K., Nishimura, M., Ikematsu, H., Yano, T., Yokota, H., 2018. Automatic detection of early gastric cancer in endoscopic images using a transferring convolutional neural network, in:. Annu. Int. Conf. IEEE Eng. Med. Biol. Soc. Annu. 40th Annual International Conference of the IEEE Engineering in Medicine and Biology Society (EMBC). IEEE Publications. 2018, 4138–4141.

Shoji, D., Noguchi, R., Otsuki, S., Hino, H., 2018. Classification of volcanic ash particles using a convolutional neural network and probability. Sci. Rep. 8, 8111.

Sibert, E., Friedman, M., Hull, P., Hunt, G., Norris, R., 2018. Two pulses of morphological diversification in Pacific pelagic fishes following the Cretaceous–Palaeogene mass extinction. Proc. Biol. Sci. 285.

Sibert, E., Norris, R., Cuevas, J., Graves, L., 2016. Eighty-five million years of Pacific Ocean gyre ecosystem structure: Long-term stability marked by punctuated change. Proc. Biol. Sci. 283.

Sibert, E.C., Cramer, K.L., Hastings, P.A., Norris, R.D., 2017. Methods for isolation and quantification of microfossil fish teeth and elasmobranch dermal denticles (ichthyoliths) from marine sediments. Palaeontol. Electron. 20, 1–14.

Sibert, E.C., Hull, P.M., Norris, R.D., 2014. Resilience of Pacific pelagic fish across the Cretaceous/Palaeogene mass extinction. Nat. Geosci. 7, 667–670.

Sibert, E.C., Rubin, L.D., 2021. An Early Miocene extinction in pelagic sharks. Science. 372, 1105–1107.

Sibert, E.C., Zill, M.E., Frigyik, E.T., Norris, R.D., 2020. No state change in pelagic fish production and biodiversity during the Eocene–Oligocene transition. Nat. Geosci. 13, 238–242.

Solano, G.A., Gasmen, P., Marquez, E.J., 2018. Radiolarian classification decision support using supervised and unsupervised learning approaches, in: 9th International Conference on Information, Intelligence, Systems and Applications (IISA) 2018. IEEE Publications, pp. 1–6.

Suleymanova, I., Balassa, T., Tripathi, S., Molnar, C., Saarma, M., Sidorova, Y., Horvath, P., 2018. A deep convolutional neural network approach for astrocyte detection. Sci. Rep. 8, 12878.

Takahashi, S., Yamakita, S., Suzuki, N., Kaiho, K., Ehiro, M., 2009. High organic carbon content and a decrease in radiolarians at the end of the Permian in a newly discovered continuous pelagic section: A coincidence?

Palaeogeogr. Palaeoclimatol. Palaeoecol. 271, 1–12.

Takaya, Y., Yasukawa, K., Kawasaki, T., Fujinaga, K., Ohta, J., Usui, Y., Nakamura, K., Kimura, J.I., Chang, Q., Hamada, M., Dodbiba, G., Nozaki, T., Iijima, K., Morisawa, T., Kuwahara, T., Ishida, Y., Ichimura, T., Kitazume, M., Fujita, T., Kato, Y., 2018. The tremendous potential of deep-sea mud as a source of rare-earth elements. Sci. Rep. 8, 5763.

Tan, M., Le, Q., 2021. Efficientnetv2: Smaller models and faster training, in: International Conference on Machine Learning, pp. 10096–10106. PMLR.

Tanaka, E., Nakamura, K., Yasukawa, K., Mimura, K., Fujinaga, K., Iijima, K., Nozaki, T., Kato, Y., 2020a. Chemostratigraphy of deep-sea sediments in the western North Pacific Ocean: Implications for genesis of mud highly enriched in rare-earth elements and yttrium. Ore Geol. Rev. 119. 103392.

Tanaka, E., Nakamura, K., Yasukawa, K., Mimura, K., Fujinaga, K., Ohta, J., Iijima, K., Nozaki, T., Machida, S., Kato, Y., 2020b. Chemostratigraphic correlations of deep-sea sediments in the western North Pacific Ocean: A new constraint on the distribution of mud highly enriched in rare-earth elements. Minerals. 10, 575.

Tanaka, E., Yasukawa, K., Nakamura, K., Ohta, J., Miyazaki, T., Vaglarov, B.S., Machida, S., Fujinaga, K., Iwamori, H., Kato, Y., 2022. Secular variations in provenance of sedimentary components in the western North Pacific Ocean constrained by Sr isotopic features of deep-sea sediments. Geochem. Geophys. Geosyst. e2021GC009729.

Tetard, M., Marchant, R., Cortese, G., Gally, Y., de Garidel-Thoron, T., Beaufort, L., 2020. Technical note: A new automated radiolarian image acquisition, stacking, processing, segmentation and identification workflow. Clim. Past. 16, 2415–2429.

Usui, Y., Yamazaki, T., Saitoh, M., 2017. Changing abundance of magnetofossil morphologies in pelagic red clay around Minamitorishima, western North Pacific. Geochem. Geophys. Geosyst. 18, 4558–4572.

Westerhold, T., Marwan, N., Drury, A.J., Liebrand, D., Agnini, C., Anagnostou, E., Barnet, J.S.K., Bohaty, S.M., De Vleeschouwer, D., Florindo, F., Frederichs, T., Hodell, D.A., Holbourn, A.E., Kroon, D., Lauretano, V., Littler, K., Lourens, L.J., Lyle, M., Pälike, H., Röhl, U., Tian, J., Wilkens, R.H., Wilson, P.A., Zachos, J.C., 2020. An astronomically dated record of Earth's climate and its predictability over the last 66 million years. Science. 369, 1383–1387.

Xu, Y., Dai, Z., Wang, J., Li, Y., Wang, H., 2020. Automatic recognition of palaeobios images under microscope based on machine learning. IEEE Access. 8, 172972–172981.

Yasukawa, K., Kino, S., Azami, K., Tanaka, E., Mimura, K., Ohta, J., Fujinaga, K., Nakamura, K., Kato, Y., 2020. Geochemical features of Fe-Mn micronodules in deep-sea sediments of the western North Pacific Ocean: Potential for co-product metal extraction from REY-rich mud. Ore Geol. Rev. 127. 103805.

Yasukawa, K., Liu, H., Fujinaga, K., Machida, S., Haraguchi, S., Ishii, T., Nakamura, K., Kato, Y., 2014. Geochemistry and mineralogy of REY-rich mud in the eastern Indian Ocean. J. Asian Earth Sci. 93, 25–36.

Yasukawa, K., Nakamura, K., Fujinaga, K., Iwamori, H., Kato, Y., 2016. Tracking the spatiotemporal variations of statistically independent components involving enrichment of rare-earth elements in deep-sea sediments. Sci. Rep. 6, 29603.

Yasukawa, K., Nakamura, K., Fujinaga, K., Machida, S., Ohta, J., Takaya, Y., Kato, Y., 2015. Rare-earth, major, and trace element geochemistry of deep-sea sediments in the Indian Ocean: Implications for the potential distribution of REY-rich mud in the Indian Ocean. Geochem. J. 49, 621–635.

Yasukawa, K., Ohta, J., Mimura, K., Tanaka, E., Takaya, Y., Usui, Y., Fujinaga, K., Machida, S., Nozaki, T., Iijima, K., Nakamura, K., Kato, Y., 2018. A new and prospective resource for scandium: Evidence from the geochemistry of deep-sea sediment in the western North Pacific Ocean. Ore Geol. Rev. 102, 260–267.

Yasukawa, K., Ohta, J., Miyazaki, T., Vaglarov, B.S., Chang, Q., Ueki, K., Toyama, C., Kimura, J.I., Tanaka, E., Nakamura, K., Fujinaga, K., Iijima, K., Iwamori, H., Kato, Y., 2019. Statistic and isotopic characterization of deep-sea sediments in the western North Pacific Ocean: Implications for genesis of the sediment extremely enriched in rare earth elements. Geochem. Geophys. Geosyst. 20, 3402–3430.

Yu, M., Shi, X., Huang, M., Liu, J., Yan, Q., Yang, G., Li, C., Yang, B., Zhou, T., Bi, D., Wang, H., Bai, Y., 2021. The transfer of rare earth elements during early diagenesis in REY-rich sediments: An example from the Central Indian Ocean Basin. Ore Geol. Rev. 136. 104269.

Yu, S., Saint-Marc, P., Thonnat, M., Berthod, M., 1996. Feasibility study of automatic identification of planktic foraminifera by computer vision. J. Foram. Res. 26, 113–123.

Zachos, J.C., Dickens, G.R., Zeebe, R.E., 2008. An Early Cenozoic perspective on greenhouse warming and carbon-cycle dynamics. Nature. 451, 279–283.

Zhang, X., Han, L., Han, L., Zhu, L., 2020. How well do deep learning-based methods for land cover classification and object detection perform on high resolution remote sensing imagery? Remote Sens. 12, 417.

Zhang, X., Tao, C., Shi, X., Li, H., Huang, M., Huang, D., 2017. Geochemical characteristics of REY-rich pelagic sediments from the GC02 in central Indian Ocean Basin. J. Rare Earths. 35, 1047–1058.

Zhou, L., Kyte, F.T., 1992. Sedimentation history of the South Pacific pelagic clay province over the last 85 million years inferred from the geochemistry of Deep Sea Drilling Project Hole 596. Paleoceanography. 7, 441–465.

Zhou, T., Shi, X., Huang, M., Yu, M., Bi, D., Ren, X., Liu, J., Zhu, A., Fang, X., Shi, M., 2021. Genesis of REY-rich deep-sea sediments in the Tiki Basin, eastern South Pacific Ocean: Evidence from geochemistry, mineralogy and isotope systematics. Ore Geol. Rev. 138. 104330.

Zhou, T., Shi, X., Huang, M., Yu, M., Bi, D., Ren, X., Yang, G., Zhu, A., 2020. The influence of hydrothermal fluids on the REY-rich deep-sea sediments in the Yupanqui Basin, eastern South Pacific Ocean: Constraints from bulk sediment geochemistry and mineralogical characteristics. Minerals. 10, 1141.

Ziegler, C.L., Murray, R.W., Hovan, S.A., Rea, D.K., 2007. Resolving eolian, volcanogenic, and authigenic components in pelagic sediment from the Pacific Ocean. Earth Planet. Sci. Lett. 254, 416–432.

List of Figures

List of Tables

2. Table S2. Results of the practical test with varying threshold confidence scores of the EfficientNet-V2 model.

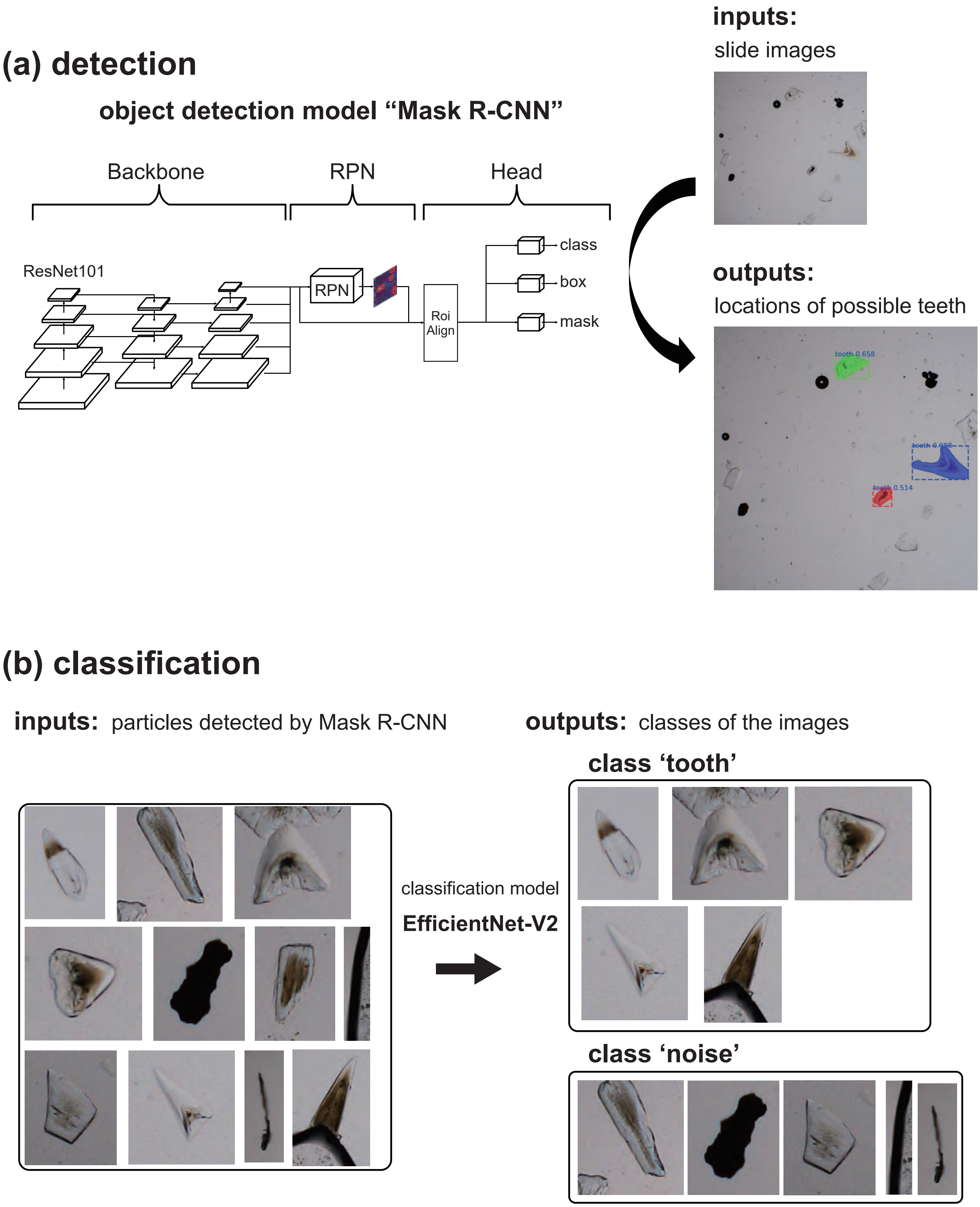
(a) detection
object detection model "Mask R-CNN"
Backbone
RPN
Head
ResNet101
RPN
Roi Align
class
box
mask
inputs:
slide images
outputs:
locations of possible teeth
tooth 0.658
tooth 0.514
(b) classification
inputs: particles detected by Mask R-CNN
outputs: classes of the images
classification model
EfficientNet-V2
class 'tooth'
class 'noise'

Figure 1

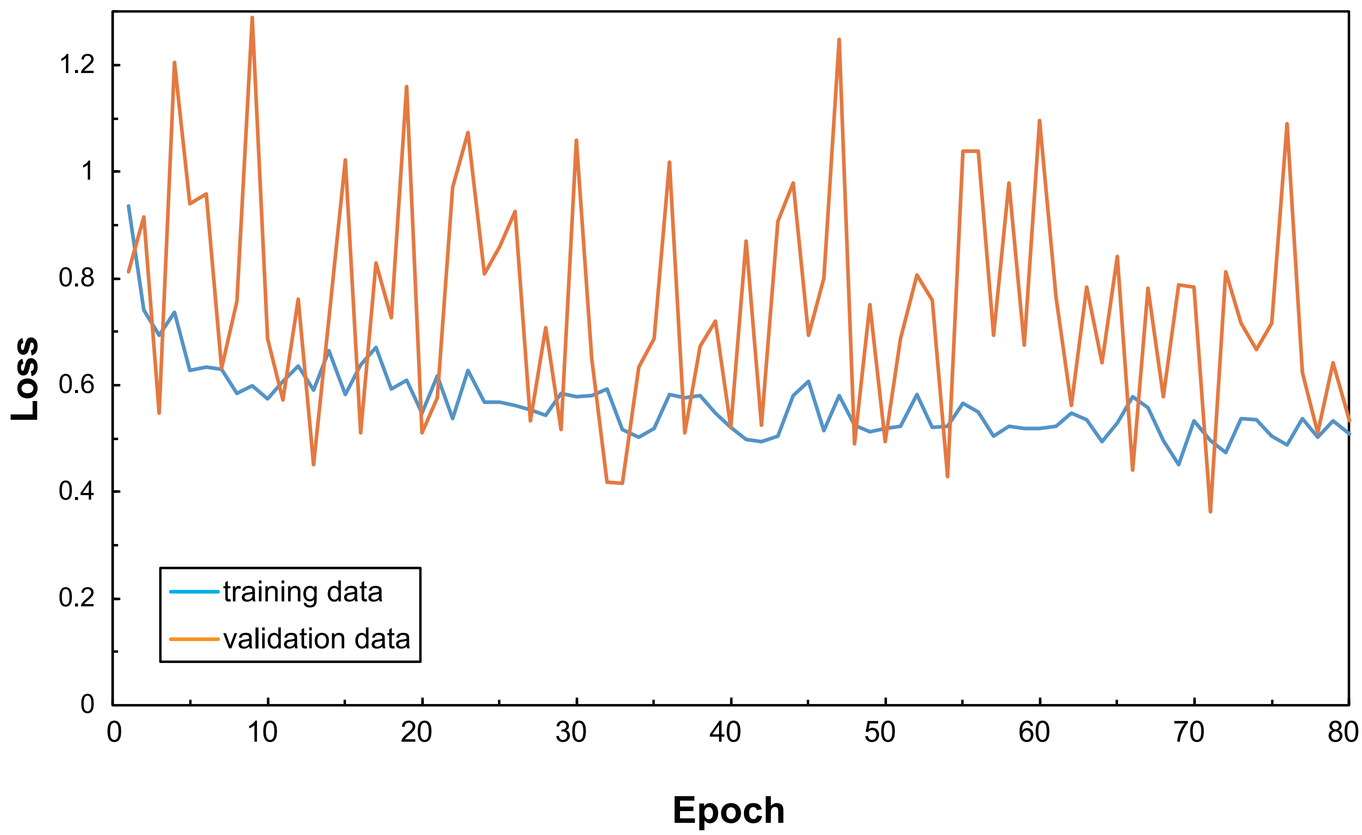

Loss
1.2
1
0.8
0.6
0.4
0.2
0
0
10
20
30
40
50
60
70
80
Epoch
training data
validation data

Figure 2

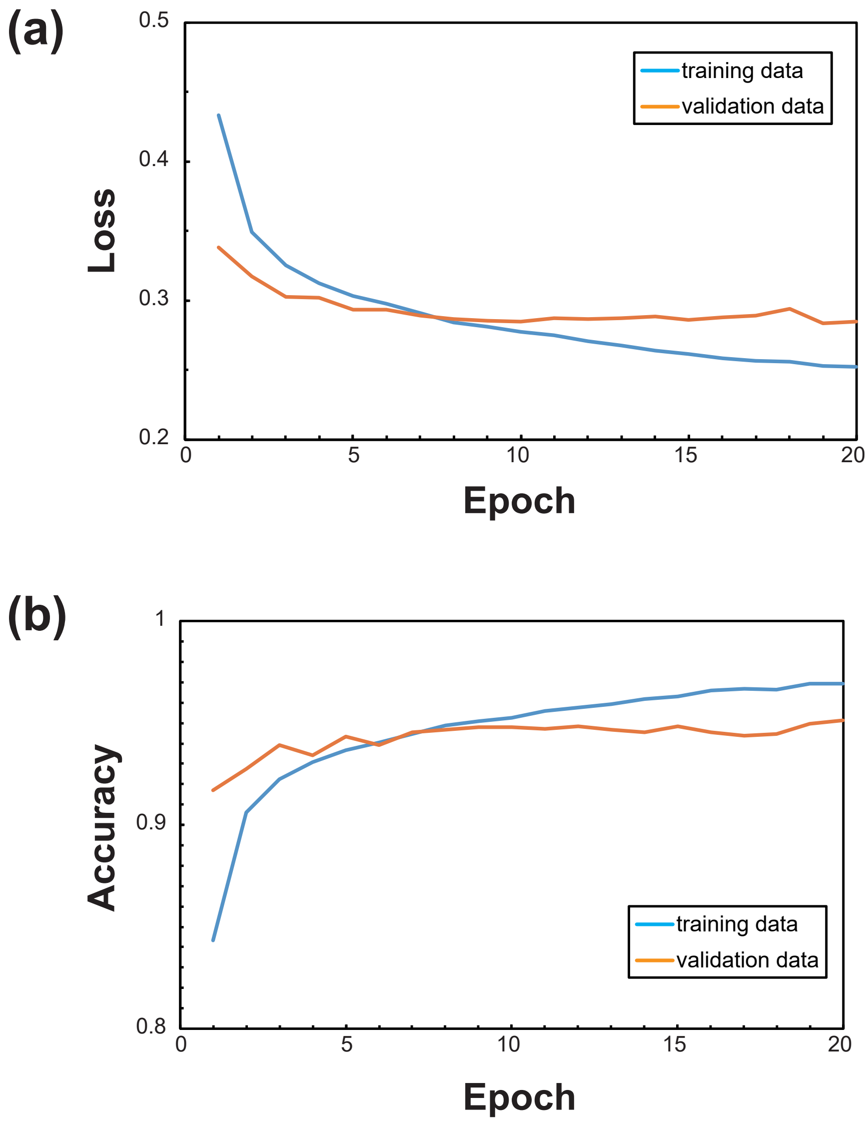

(a)
0.5
0.4
0.3
0.2
Loss
0
5
10
15
20
Epoch
training data
validation data
(b)
1
0.9
0.8
Accuracy
0
5
10
15
20
Epoch
training data
validation data

Figure 3

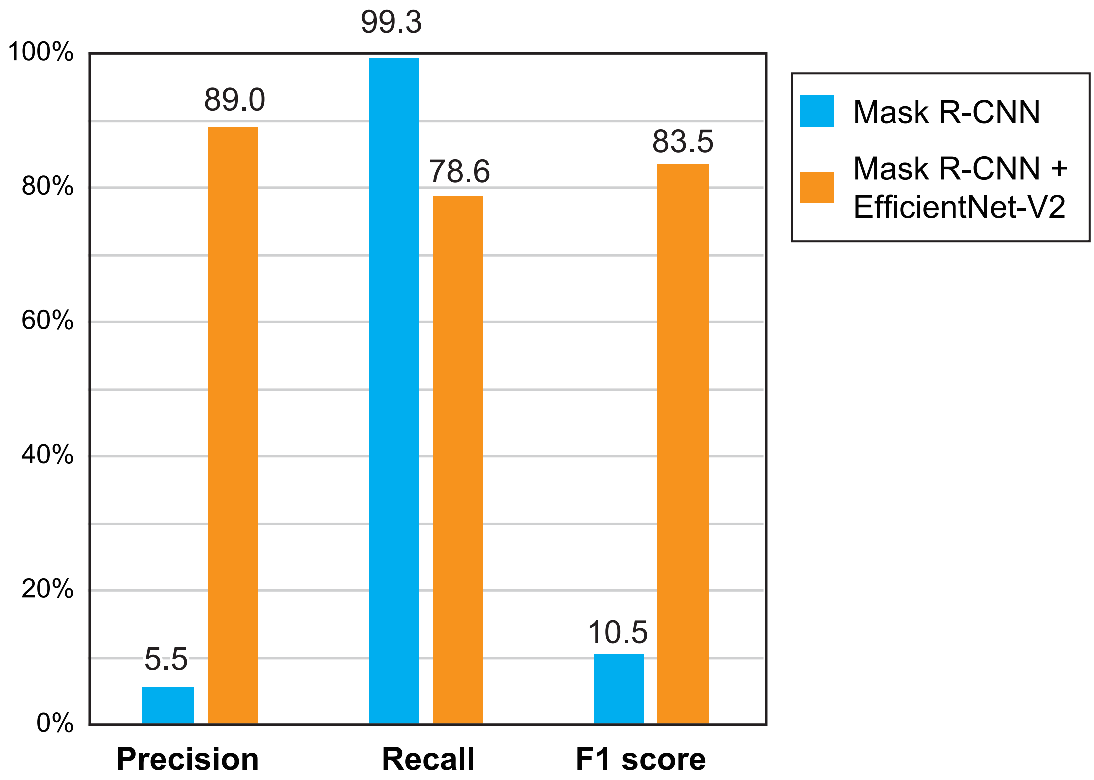
100%
80%
60%
40%
20%
0%
99.3
89.0
78.6
83.5
5.5
10.5
Precision
Recall
F1 score
Mask R-CNN
Mask R-CNN + EfficientNet-V2

Figure 4

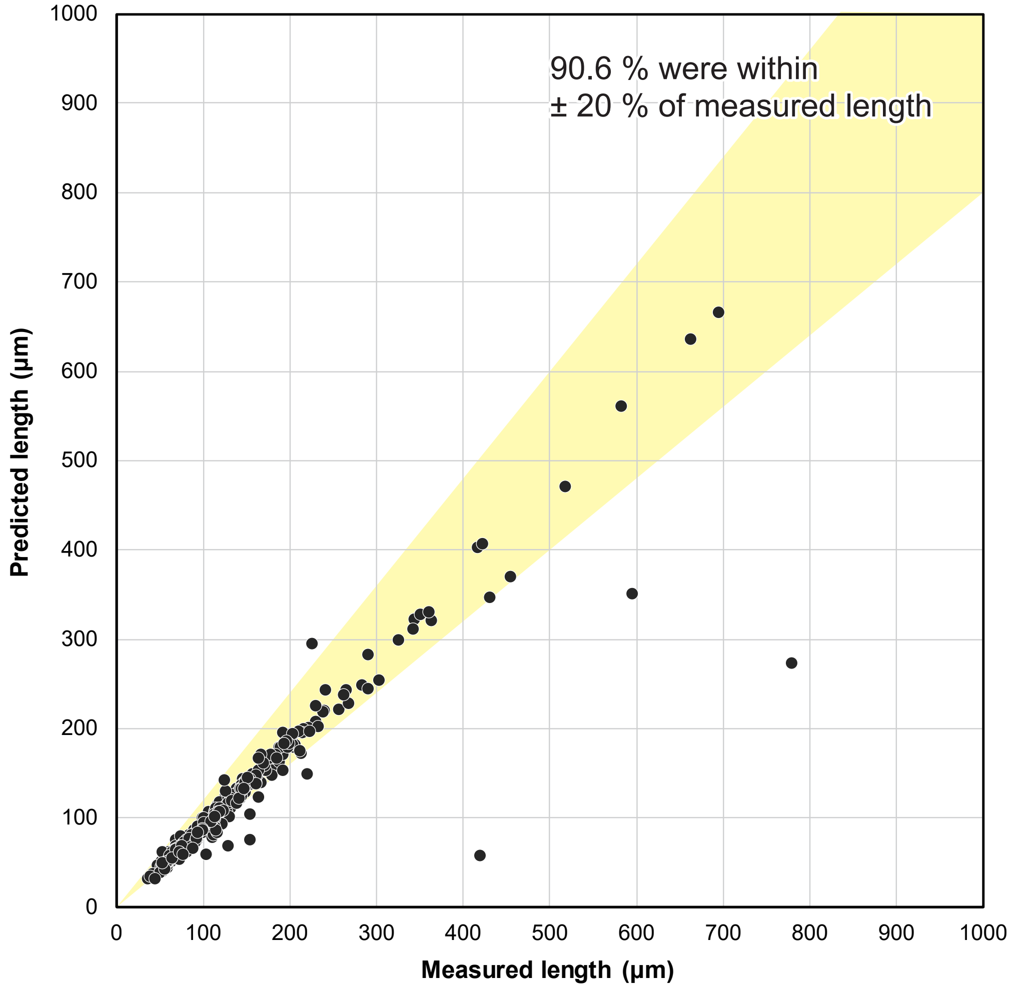

90.6 % were within
± 20 % of measured length
Predicted length (µm)
Measured length (µm)
0
100
200
300
400
500
600
700
800
900
1000

Figure 5

(a) Manually measured length

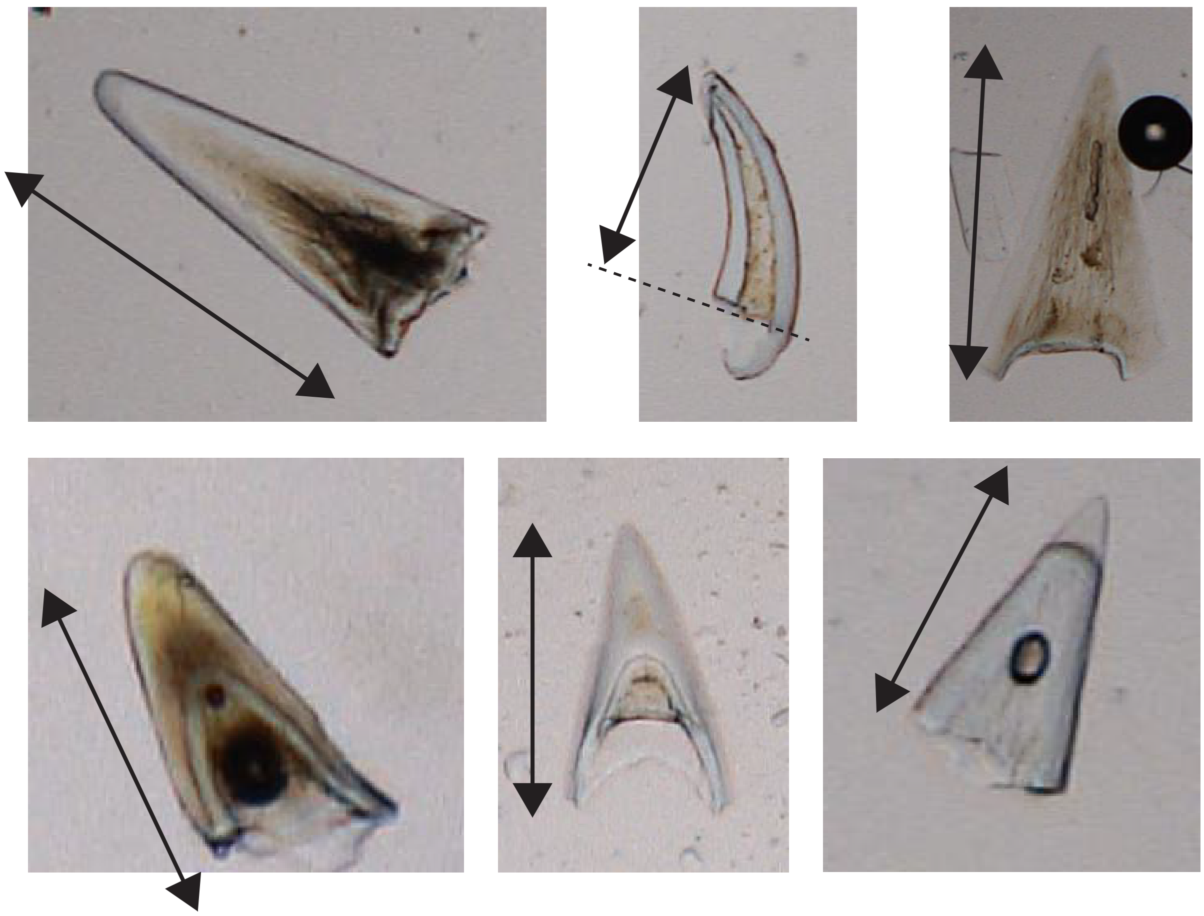

(b) Prediction of length by contour

contour predicted by Mask R-CNN model

The smallest rectangle that encloses a contour

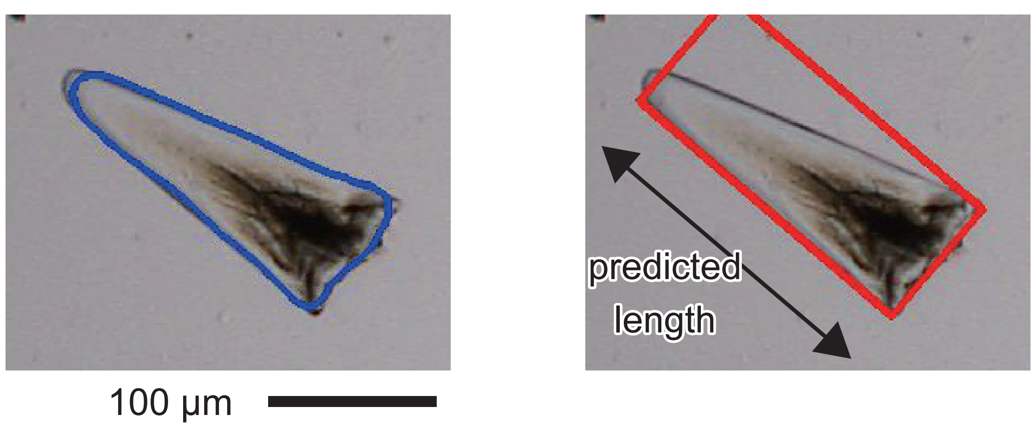

Figure S1

Table S1. Locations and water depths of the analyzed sites.

ODP/DSDP	Leg/Cruise	Site	Hole	Latitude	Longitude	Water depth [m]
ODP	191	1179	C	41°04.7871' N	159°57.7856' E	5,563.9
IODP	Exp. 329	U1366	C	26°03.0845' S	156°53.6700' W	5,129.5
		U1370	D	41°51.1156' S	153°06.3812' W	5,073.0
-	MR15-E01	PC11	-	21°58.2732’ N	153°47.7461’ W	5,770

Table S2. Results of the practical test with varying threshold confidence scores of the EfficientNet-V2 model.

threshold score	Recall	Precision	F1 value
0.1	90.8	61.9	73.6
0.15	86.4	74.1	79.8
0.2	84.8	79.0	81.8
0.25	83.2	81.1	82.1
0.3	80.9	82.8	81.8
0.35	80.2	85.1	82.6
0.4	79.0	87.3	83.0
0.45	**78.6**	**89.0**	**83.5**
0.5	77.6	89.9	83.3
0.55	77.4	90.3	83.4
0.6	76.3	91.4	83.2